

Volumetric parcellation of the cardiac right ventricle for regional geometric and functional assessment.

Bernardino, G^{1,*}, Hodzic, A^{2,3,*}, Langet, H⁴, Legallois, D⁵, De Craene, M⁴,
González Ballester, MA^{1,6}, Saloux, E⁵, and Bijmens, B^{6,7,8}

¹BCN Medtech, Dept. of Information and Communication Technologies,
Universitat Pompeu Fabra, Barcelona, Spain

²Department of Clinical Physiology, CHU Caen - Normandie, Caen, France

³Normandie Univ, UNICAEN, Caen, France

⁴Philips Research, Paris, France

⁵Department of Cardiology, CHU Caen - Normandie, Caen, France

⁶ ICREA, Barcelona, Spain

⁷ IDIBAPS, Barcelona, Spain

⁸ KULeuven, Leuven, Belgium

May 29, 2022

Abstract

3D echocardiography is an increasingly popular tool for assessing cardiac remodelling in the right ventricle (RV). It allows quantification of the cardiac chambers without any geometric assumptions, which is the main weakness of 2D echocardiography. However, regional quantification of geometry and function is limited by the lower spatial and temporal resolution and the scarcity of identifiable anatomical landmarks. We developed a technique for regionally assessing the 3 relevant RV regions: apical, inlet and outflow.

The method's inputs are end diastolic (ED) and end systolic (ES) segmented 3D surface models, in point-to-point correspondence obtained by tracking. The method first defines a partition of the ED endocardium using the geodesic distances from each surface point to apex, tricuspid valve and pulmonary valve: the landmarks that define the 3 regions. The ED surface mesh is then tetrahedralised, and the endocardial-defined partition is interpolated in the blood cavity via the Laplace equation. For obtaining an ES partition, the endocardial partition is transported from ED to ES using a commercial image-based tracking, and then interpolated towards the endocardium, similarly to ED, for computing volumes. Additionally to the volumes, we derive regional ejection fraction (EF) to assess segmental cardiac function.

We present a full assessment of the method's validity and reproducibility. First, we assess reproducibility under segmentation variability, obtaining intra- and inter- observer errors (4 – 10% and 10 – 23% resp.). Finally, we use a synthetic remodelling dataset to identify the situations in which our method is able to correctly determine the region that has remodelled. This dataset is generated by a novel mesh reconstruction method that deforms a reference mesh, locally imposing a given strain, expressed in anatomical coordinates. We show that the parcellation method is adequate for capturing local circumferential and global circumferential and longitudinal RV remodeling, which are the most clinically relevant cases.

1 Introduction

Cardiac myocytes thicken and/or elongate (Arts et al., 1994; Grossman et al., 1975; Opie et al., 2006) as a reaction to altered stimuli (such as pressure or volume loading). These cellular changes are aggregated at organ level, producing size and shape changes in the heart chambers and affecting cardiac function. This process is commonly referred to as cardiac remodelling. Adaptive remodelling helps the heart to pump enough blood to satisfy the system oxygen demands while maintaining pressure within physiological range. Maladaptive remodelling results in changes that are either not sufficient to compensate altered situations, or start damaging the heart, ultimately making it unable to satisfy the systemic oxygen demands and fail.

Even if remodelling results from adaptation of individual myocytes as a response to very local stimuli, in clinical practice it is often simplified to global changes: a wall thickening with inward motion of the inner wall (thus reducing cavity size and wall stress) as a reaction to pressure loading and a dilatation of the cavity to cope with volume overload, so that, without changing the wall deformation during contraction, more stroke volume is ejected with each beat. However, many conditions have been described to produce regional remodelling: such as for instance the presence of a basal septal bulge induced by hypertension Baltaeva et al. (2007), a thickening of the septal wall in hypertrophic cardiomyopathies (Olivotto et al., 2012) or a base-to-apex gradient in deformation in deposition diseases such as amyloidosis (Cikes et al., 2010) or thalassemia (Hamdy, 2007). In the clinical community, the quantification of regional patterns is mostly used in segmental motion and deformation assessment (particularly in coronary artery disease) rather than local geometry. For the left ventricle (LV), a standardised partition in 17 wall segments has been proposed (Cerqueira et al., 2002), which recently also has been used to quantitatively assess regional strain patterns. However, these wall segments are by definition equal in size and thus of limited utility to assess changes in morphology.

In medical image analysis, a common method to quantify regional morphology is through the creation of an *atlas*, which is a template shape representative of a population, and registering each patient-specific shape to this atlas (Zhang et al., 2017). This has shown to be useful to describe inter-individual variations of overall morphology in populations, but is more challenging when following subtle regional remodelling within an individual over time, since the use of an atlas regularizes and smooths the data. Additionally, this approach has the drawback that it requires registration (deforming the atlas to match the individual) (Joshi et al., 2004). Registration remains an unstable and computationally expensive process, even if there has been advances to ease both the stability and computation time (Benkarim et al., 2019; Fu et al., 2019). A particular problem of the cardiac right ventricle (RV) is that there are few and separated landmarks that can be identified among different individuals: registration is based on image intensity/shape patterns, and has no guarantee of the correctness of the point-to-point correspondence. Thus, when using computational meshes to represent the heart through image segmentation, after atlas registration, an important part of the mesh nodes' positions do not correspond to identifiable anatomic landmarks among different individuals so that point-to-point correspondence cannot be used anymore to assess specific physiological remodelling associated with local stimuli.

To avoid explicit registration, some authors have proposed parametrisation methods to create anatomical maps of organs (Nuñez-Garcia et al., 2019; Vera et al., 2014; Paun et al., 2017; Auzias et al., 2013; Hurdal and Stephenson, 2009) by finding smooth bijective maps from each surface/volume to a common domain, a subset of \mathbb{R}^2 or \mathbb{R}^3 respectively. The parametrisations of individual anatomies can subsequently be used to obtain a point-to-point correspondence. The mapping is typically obtained through a minimisation of a distortion metric. In particular, several authors propose to force the mapping to be as conformal as possible, ie locally maintaining angles, (Lévy, 2001; Gu et al., 2010). Maintaining angles is not the only possibility: there are

other approaches that try to maintain, for instance, local distances (Sorkine and Alexa, 2007) or areas.

Compared to the LV, the RV has a complex and irregular shape, with more segmental variability (Haddad et al., 2008a) so that regional analysis of the RV is more difficult than of the LV. Its position in the chest also produces a bad acoustic window when using 3D echo-cardiography and results in low-quality images, limiting the applicability of complex techniques. Instead, in clinical research, a segmental approach is more common due to its easier interpretability and the spatial smoothing effect of averaging over the segment. There have been studies referring to a regional analysis of different segments that compose the RV (Addetia et al., 2016, 2018; Moceri et al., 2018). These studies only analyse the endocardium, more specifically its wall curvature. While local curvature is an important component of the wall stress generated by pressure and thus very important in pressure-overload remodelling, an analysis in terms of regional dilatation/volume is needed to correctly assess remodelling from volume-overload. Therefore, there is a need for quantitative approaches that can assess regional shape, as well as volume, remodelling in a clinically relevant and physiologically plausible way.

In this paper we develop a segmental analysis tool suitable for a clinical application, using images of suboptimal quality, by proposing an automatic method for mesh-independent volumetric parcellation of the RV based on the geodesic distance to three easily identifiable anatomical landmarks: tricuspid valve, pulmonary valve and apex. Complementarily, in order to assess the method’s potential to identify clinically relevant and physiologically plausible regional remodelling, we propose a method to generate synthetic datasets through regional induction of circumferential and longitudinal elongation and analyse the sensitivity of the parcellation to both global and regional remodelling. To assess the performance, and robustness to noise, in a real setting, we also do an inter- and intra- observer reproducibility analysis, as well as a test/retest comparison of two sequential acquisitions, on the same patient. This technique enables both a regional analysis of anatomy, using the end diastolic (ED) volumes, as well as function, via regional ejection fraction (EF).

2 Methodology

2.1 Parcellation of the right ventricle

The RV has a complex and asymmetric shape and is positioned partly surrounding the LV. Its anatomy is most commonly described as biaxial: one axis goes from tricuspid valve to the apex, and the other from the apex to the pulmonary valve. The RV can grossly be separated in 3 main anatomically and functionally different parts: the outflow infundibulum, the smooth inlet and the trabeculated apex (Haddad et al., 2008a,b). However, there is no consensus on the exact border between these parts, and different experts can draw different region boundaries over the same images. Given that the partition definition is needed to quantify volume and shape changes over time when doing follow-up in individuals, we propose an automatic method for volumetric parcellation of the RV, based only on geometric properties. While this partition has the advantage of being fully automatic and therefore completely reproducible under the same image and segmentation, the method still relies in the generated 3D model thus depending on the original segmentation quality and stability. To avoid errors due to a bad point-to-point correspondence, our parcellation does not use explicit registration and only uses the geodesic distances from anatomic landmarks that can be clearly identified in 3D echocardiography: the apex, tricuspid and pulmonary valve. The method is independent of the exact triangulation of the ventricular surface.

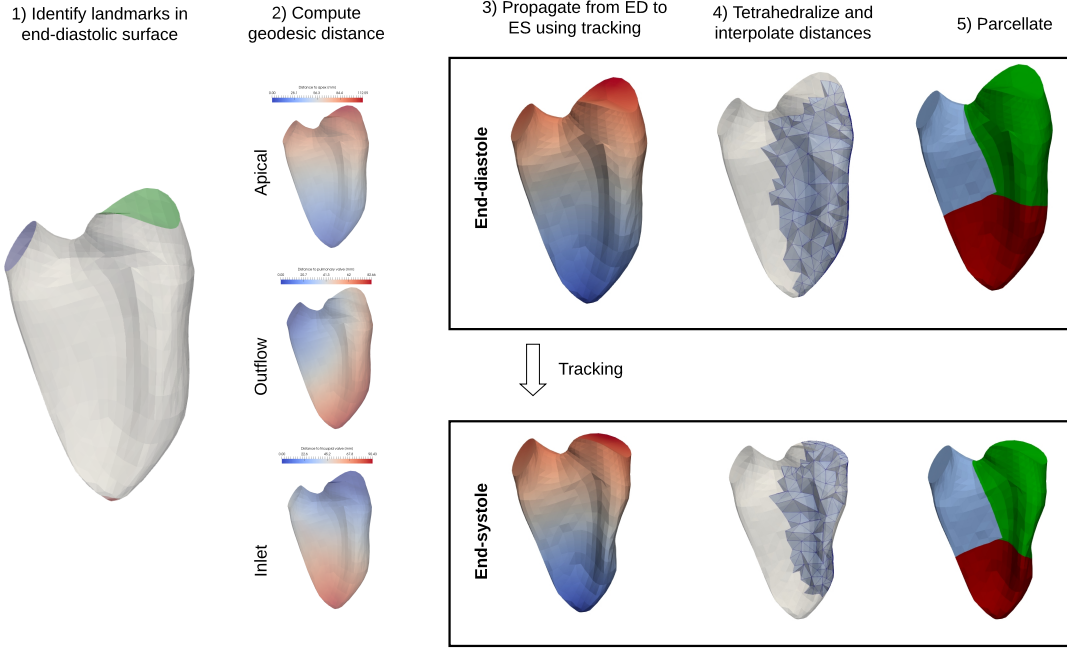


Figure 1: Steps to generate the volumetric partition. 1-2) For each point of the ED surface, the geodesic distances to the apex, tricuspid and pulmonary valves are computed and define a scalar map. 3) The maps are propagated from ED surface to ES surface following the tracking 4) This distance map is extended from the surface to the cavity by tetrahedralising the ED and ES meshes, and the Laplace equation is used to interpolate values to the interior. 4) The ventricle is split in the regions by assigning each point of the cavity to the closest landmark.

We applied our method to the analysis of 3D models of the RV generated from 3D echocardiography images using Tomtec software (4D RV-FUNCTION), but it can easily be adapted to other processing platforms and imaging modalities. This software provides a semi-automatic model-based segmentation of the RV, and a tracking during the full cardiac cycle. Figure 1 shows the full process used to parcellate the RV, which is described below.

The first step of our parcellation is the identification of the valves and apex using the point-to-point correspondence provided by the semiautomatic segmentation software in the endocardial surface mesh (given that these correspond to stable anatomical landmarks in the mesh that can be identified in the image). Next, for each node of the mesh, we compute the geodesic distances to the apex, pulmonary valve and tricuspid valve. The geodesic distances between two points are computed on the surface with an exact algorithm (Surazhsky et al., 2005) that computes the length of the minimal on-surface path between two points. The distance between a point and an anatomical substructure is defined as the minimum distance from the point to any point that belongs to that anatomical substructure:

$$\begin{aligned}
 d_t(x) &= \min\{d_{geo}(x, y) | y \in \text{tricuspid valve}\} \\
 d_p(x) &= \min\{d_{geo}(x, y) | y \in \text{pulmonary valve}\} \\
 d_a(x) &= \min\{d_{geo}(x, y) | y \in \text{apex}\}
 \end{aligned} \tag{1}$$

Figure 1.a shows the geodesic path from an arbitrary point to the different landmarks, and

Figure 1.b shows distance from every point of the surface to the apex represented as a heatmap: the points furthest to the apex are coloured in red and the closest in blue. After this distance is computed for every point of the surface, the interior of the triangular surface mesh is tetrahedralised using a publicly available software (TetGen version 1.5.1, Si (2015)) (Figure 1.c). The distance defined on the surface of the mesh is propagated to the interior of the ventricle using Laplace's equation. The equation uses the tetrahedralised mesh as domain and Dirichlet boundary conditions specified by the surface-defined distance maps. Formally, this interpolation step is defined as follows, where $M \in \{apical, inlet, outflow\}$, Ω refers to the volumetric domain and $\partial\Omega$ and $\mathring{\Omega}$ to its boundary (the surface mesh) and interior respectively:

$$\begin{cases} \Delta u_M = 0 & \text{for } x \in \mathring{\Omega} \\ u_M(x) = d_M(x) & \text{for } x \in \partial\Omega \end{cases} \quad (2)$$

This equation is discretised using finite elements with a publicly available software (Sfepy Cimrman et al. (2019)). This process is repeated to compute and extend to the interior of the cavity the 3 distances. Once the distances are defined in the volumetric mesh, we partition the ventricle, assigning each point of the mesh to the "closest" landmark, using the interpolated distances. M_{inlet} , M_{apical} and M_{outlet} respectively, are the partition corresponding to the inlet, apex and outlet. Each point is assigned to the region whose representing landmark is closer as shown in Figure 1.4. The partition does not follow the mesh vertices and edges, but new elements are generated during the partition. We used linear interpolation to define the distance values inside each tetrahedron. A formal definition of the segments is:

$$M_{inlet} = \{x | d_t(x) \leq d_p(x), d_t(x) \leq d_a(x)\} \quad (3)$$

$$M_{outlet} = \{x | d_p(x) \leq d_t(x), d_p(x) \leq d_a(x)\} \quad (4)$$

$$M_{apical} = \{x | d_a(x) \leq d_t(x), d_a(x) \leq d_p(x)\} \quad (5)$$

This partition can be propagated from the ED-surface to end systolic (ES)-surface using the point-to-point correspondence between surfaces belonging to the same individual, that are obtained via tracking the initial surface, and then extended to the interior cavity via the same Laplacian interpolation. With this procedure, we can compute regional ES volumes and ejection fractions, allowing for regional functional assessment of the RV.

2.2 Local and global anatomic frame of reference

To clinically interpret local geometric changes, it is more convenient to work in an anatomical frame of reference, with longitudinal and circumferential directions, instead of the Cartesian system of coordinates. At each point of the mesh, circumferential and longitudinal directions are defined locally using the method proposed by Doste et al. (2019). We defined the longitudinal direction using the stationary heat flow in surfaces, with a cold source in the apex, and two hot sources at the same temperature in the two valves. The heat flow is computed by solving the Laplace-Beltrami linear differential equation on a surface. The Laplace-Beltrami operator (Δ) is discretised using the cotangent formulation (Pinkall and Polthier, 1993):

$$\begin{cases} \Delta u = 0 \\ u(apex) = 0 \\ u(valves) = 0 \end{cases} \quad (6)$$

The longitudinal direction (l) at each point is the result of normalising the resulting temperature gradient. The circumferential (c) is chosen to be orthogonal to both the longitudinal and

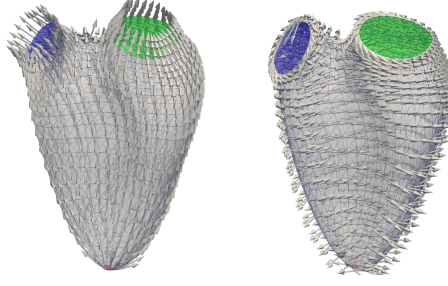


Figure 2: Longitudinal (right) and circumferential (left) directions defined in each triangle of a sample RV mesh. The tricuspid valve is shown in green and the pulmonary valve in blue. Since valves are not part of the myocardium, the definition of the anatomical direction there has no meaning.

the surface normal at that point (n), so that (l, c) form a base of the tangent space at the given point:

$$l = \frac{\nabla u}{\|\nabla u\|} \quad (7)$$

$$c = l \times n \quad (8)$$

Figure 2 shows the local circumferential and longitudinal directions. A global longitudinal direction is computed by averaging all the local ones, and the circumferential directions are defined as orthogonal to the longitudinal.

2.3 Remodelling deformation strain

For two meshes, a reference and a remodelled mesh, in point-to-point correspondence, we can compute the strain associated to the remodelling. This strain fully characterises the deformation, modulo rigid body transformations. To interpret this strain, it is more natural to work in the previously defined local anatomical reference frame. For each triangle, we can express each of its edges as a combination of the local anatomical directions (l, c) . We note E_t^m the matrix that contains the edges of triangle t and mesh m . With this, we can compute the local linear transformation F_t at triangle t . In a continuous setting, this F_t corresponds to the Jacobian matrix of the deformation.

$$F_t = E_t^{m_{def}} (E_t^{m_{ref}})^{-1} \quad (9)$$

From this transformation, we can compute the Cauchy strain tensor for small displacements $\epsilon = (F^t + F)/2$, and extract the strain in the longitudinal (ϵ_{ll}) and circumferential (ϵ_{cc}) directions. Note that longitudinal and circumferential directions are not necessarily aligned to the principal strain directions, which are the eigenvectors of the strain tensor.

2.4 Generation of synthetic remodeling patterns

To test our algorithm, we deform a real mesh with a prescribed strain, obtaining a synthetic remodelled mesh for which we know which are the areas that have change from the reference, and with which magnitude. This is achieved by solving an inverse problem of the forward strain calculation defined in the previous section. We used a modification of a linear surface construction

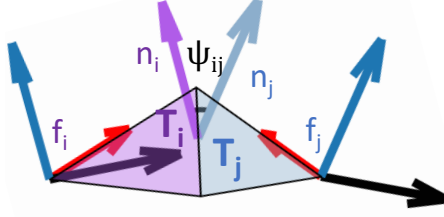


Figure 3: Two adjacent triangles T_i and T_j , with their respective local systems of reference, f_i and f_j . ψ_{ij} is the dihedral angle, represented at the mean point of the common edge, which is the angle formed between the two normals (n_i, n_j).

method (Wang et al., 2012) that generates 3D meshes from a local description. The remodelled mesh connectivity is an input of the method and it cannot contain a non-manifold edge. The local description consists of the edge lengths and the dihedral angle associated to every edge (the angle formed by the normals of the adjacent triangles). Obviously, not all combinations of lengths and angles define a valid surface, but we can formulate the reconstruction in a minimisation setting so we obtain the surface satisfying as much as possible the local description. We will use this method to simulate remodelling, by locally deforming a template mesh.

2.4.1 Local descriptors of the surface

We describe a local frame of reference for each triangle of the mesh from the input data. This frame is arbitrary but uniquely defined, assuming a unique ordering of the nodes inside each triangle. It uses the first node of the triangle as origin, the direction of the first edge as x-axis, the normal as the z-axis and then completes the base to be orthonormal. We will call $a_{t,i}$ the coordinates of the i -th point of the t -th triangle expressed in local frame. By convention, $a_{t,0} = (0,0,0)$, the third coordinate is always 0 for all points (since they are coplanar), and $a_{t,1} = (x,0,0)$. Note that by basic trigonometry we can compute the local coordinates of the triangle nodes given the 3 lengths, using the constraints that the first node is in 0, and the second one lies in the x-axis.

The unknown variables are the 3D coordinates x_i for each mesh point i , and a reference frame f_t associated to each triangle t , that corresponds to the mapping from the triangle coordinates a to the 3D space. Figure 3 shows two adjacent triangles, with their dihedral angle and the associated frames of reference.

For two adjacent triangles i and j , we can obtain the rotation R_{ij} from frame f_j to f_i :

$$R_{ij} = f_j^T f_i \quad (10)$$

We can express R_{ij} using only the local descriptor: the triangle coordinates and the dihedral angles ψ_{ij} . We call ϕ_v^θ the rotation of angle θ around the axis of rotation v . Let e be the common edge between triangles T_i and T_j , we can compute the angle θ between edge e and the first edge of T_i , and θ' is the respective angle for T_j . Then, we can express R_{ij} as the composition of 3 rotations:

$$R_{ij} = \phi_z^{\theta'} \phi_x^{\psi_{ij}} \phi_z^\theta \quad (11)$$

2.4.2 Linear reconstruction

In this section we formulate the inverse problem to generate a mesh using the previously defined variables R and a . Given a mesh topology, and values for the dihedral angles and edge lengths defined at each edge and face respectively, the algorithm finds a 3D mesh that satisfies as much as possible the desired local geometry. We manipulate the forward equations of the preceding section to obtain an equivalent form linear on x and f , and use their quadratic residual as energy to minimize, thus formulating an optimisation problem with the world position of the nodes x and the frames f as variables. To easily solve this problem, we do not enforce that matrices f are rotations, but arbitrary matrices.

By multiplying by f_j equation 10 and rearranging terms, we obtain the following equivalent equation:

$$f_i - f_j R_{ij} = 0 \quad (12)$$

For every edge e_{ij} in every triangle t , where the nodes have in-triangle indices i' and j' respectively, we can use that f_t to transform from triangle coordinates to world coordinate:

$$x_i - x_j = f_t (a_{ti'} - a_{tj'}) \quad (13)$$

After moving all terms to the LHS, we obtain:

$$x_i - x_j - f_t (a_{ti'} - a_{tj'}) = 0 \quad (14)$$

Thus, we have obtained equations for computing x and f from R and a . We create an energy by minimising the squared L_2 error of the sum over all edges of equations 12 and 14. For the matrices we use the Frobenius norm, which is simply the sum of squares of all the elements. We can add weights to each term of the equation (the one that solves for the frames, and the one that solves for the node position) to control their relative contribution to the global solution. This energy is quadratic and sparse, so it can be efficiently solved with linear methods via its normal equations. Its final form reads:

$$W_I(x, f) = \sum_{ij \in E} \sum_{\forall t - ij} \|x_i - x_j - f_t(a_{ti'} - a_{tj'})\|^2 \quad (15)$$

$$W_{II}(f) = \sum_{ij \in E} \|f_i - R_{ij} f_j\|^2 \quad (16)$$

$$W = \lambda_1 W_I + \lambda_2 W_{II} \quad (17)$$

Where E is the set of edges of the mesh, and the predicate $t - ij$ denotes that the face t is adjacent to edge ij and $a_{ti'}$ (respectively $a_{tj'}$) denotes the in-triangle coordinates of node i (respectively j) in face t . Since the meshes obtained from the segmentation were very regular, we have set both λ_1 and λ_2 to 1.

2.4.3 Log-domain reconstruction

In the previous formulation, it is not imposed that frames f exactly correspond to orthonormal matrices. This can lead to a degenerate solution where all f have a determinant < 1 and the mesh is shrank. To avoid this situation, a solution is to enforce that matrices f are rotations by parametrising them on an appropriate domain.

Any scalar analytic function can be converted to a matricial function, by using the matrix multiplication instead of the usual multiplication to compute the powers of the variable in the Taylor series of the function. Therefore, the matrix exponential is defined as:

$$\exp(X) = \sum_n \frac{X^n}{n!} \quad (18)$$

A well known result is that the matrix exponential of a matrix A is a rotation if and only if A is antisymmetric, so, we can make $f_i = \exp(w_i)$, where w_i is an antisymmetric matrix. An antisymmetric matrix can be parametrised by its 3 lower triangular components. We define $[v]_\times$ as the mapping from the parameters v to the associated antisymmetric matrix, where $v \in \mathbb{R}^3$:

$$[v]_\times = \begin{pmatrix} 0 & -v_3 & v_2 \\ v_3 & 0 & -v_1 \\ -v_2 & v_1 & 0 \end{pmatrix} \quad (19)$$

This parametrization disrupts the linearity of the previous energy (Eq 15), but we are still able of computing the derivatives. Usually matrix functions are very cumbersome to differentiate, but for the particular case of the matrix exponential of a 3D antisymmetric matrix, there exists a closed formula (Gallego and Yezzi, 2015). Specifically, when applied to a fixed vector u , and using the notation $f(v) = \exp([v]_\times)$, where v are the reduced parameters of an antisymmetric matrix:

$$\frac{\partial f(v) \cdot u}{\partial v} = -f(v)[u]_\times \frac{vv^T + (f(v)^T - Id)[v]_\times}{\|v\|^2} \quad (20)$$

Using the derivative formula of the matrix exponential, and standard matrix calculus we find the derivatives of the previous expressions. We use the trick that, for any orthonormal base (e_0, e_1, e_2) and any matrices $A, B \in \mathbb{R}^{3 \times 3}$:

$$\langle A, B \rangle_F = \sum_k \langle Ae_k, Be_k \rangle \quad (21)$$

The first dot product is the Frobenius product between matrices, and the second is the usual dot product between vectors. With this trick, we can compute the derivatives for each rotation defined over a face f_i , and each node position x_i . We note as $D(v)[u]$ the derivative $\frac{\partial f(v)u}{\partial v}$ to avoid a cumbersome notation. After some trivial computations and reordering, we obtain:

$$f_i = \exp(v_i) \quad (22)$$

$$\begin{aligned} \nabla_{f_i} W_I(v, x) = \\ 2 \sum_k \sum_{ij \in E} D(f)[e_k] (f_{t_i} e_k - R_{ij} f_{t_j} e_k) \end{aligned} \quad (23)$$

$$\begin{aligned} \nabla_{f_i} W_{II}(v, x) = \\ 2 \sum_{e=(u,v) \in t_i} D(f)[a'_u - a'_v] (x_u - x_v - f(a'_u - a'_v)) \end{aligned} \quad (24)$$

$$\nabla_{x_i} W_I(v, x) = 2 \sum_t \sum_{e=(i,j)-i} \langle x_i - x_j - f_t(a'_i - a'_j) \rangle \quad (25)$$

$$\nabla_{x_i} W_{II}(v, x) = 0 \quad (26)$$

Where t_i and t_j refer to the faces of node i and j respectively, that are adjacent to the edge ij . Since we can analytically compute the gradient, we can use a first order optimisation method. We use the L-BFGS quasi-Newton algorithm (Dennis and Moré, 1977; Nocedal, 1980).

2.4.4 Global remodelling

Global remodelling involves large changes that correspond to overall size rather than the local shape remodelling. It corresponds to the variability due to for instance the individual's height and weight. Even though it could be generated using the previous method, a simple affine transformation applied to the reference mesh nodes coordinates is enough to model this remodelling. First, we define the global longitudinal direction l_{glob} as the average of the local longitudinal direction, and the circumferential directions are defined as orthogonal to the longitudinal. The longitudinal and circumferential remodelling transformations are modelled as linear function for each $t \in \mathbb{R}$, which is the factor of stretching in the desired direction. The longitudinal transformation is defined as $(Id + t * l_{glob} \otimes l_{glob})$, and the circumferential as $(Id + \sqrt{t} * (Id - l_{glob} \otimes l_{glob}))$, where Id is the 3×3 identity matrix, \otimes is the Kroencker product and t the scaling parameter that controls the increase in volume.

3 Experimental setting

3.1 Data acquisition

3D echocardiographic images of 10 male subjects were acquired in a modified apical 4 chambers view using an EPIQ7 ultrasound system (Philips Medical Systems, Andover, MA, USA) equipped with a 1 to 5 MHz transthoracic matrix array transducer (X5-1). For each patient, 4-6 different ECG-gated subvolumes were acquired in a single breath-hold to be compounded into the full 3D+t images of 2 complete cardiac cycles. A written informed consent form was obtained from all study participants.

Another male subject was imaged in two consecutive acquisitions by two different operators to obtain an estimate of the variability due to the imaging process.

The image loops were processed using a clinically validated software (4D RV-FUNCTION Tomtec-Arena TTA2, Tomtec Imaging Systems GmbH, Unterschleissheim, Germany (Niemann et al., 2007; Muraru et al., 2016)) to segment and track the RV and obtain a 3D-model for each patient. These models were exportable in *ucd*, a standard file format. All 3D models had the same topology: a triangular watertight mesh with 938 nodes and 1872 faces. The points were in approximate point-to-point correspondence among different individuals. The segmentation pipeline consisted of the following steps: first the clinician segments the RV endocardium contour of the frame corresponding to the R peak using the semiautomatic tool, and the result is tracked during a full cycle. Afterwards, the clinician can adjust the ES and ED (defined as the peak of the R wave in the ECG) segmentation iteratively until visually satisfied with the resulting contours.

3.2 Reproducibility of the semiautomatic segmentation

We analysed the reproducibility of the RV segmentations of the 3D-echocardiographic images processed using Tomtec. For each subject, the same image loops were requantified 3 times for each acquisition by two different operators, to assess the inter- and intra-observer repeatability of the resulting surfaces and their point-to-point correspondence. For each pair of re-analysed surfaces derived from the same images, we computed the difference of global volumes and the Dice coefficient of the different segmentations, a standard measure for comparing two different segmentations (noted as S_1 and S_2) and defined as:

$$Dice(S_1, S_2) = \frac{2|S_1 \cap S_2|}{|S_1| + |S_2|} \quad (27)$$

As a measure of the mesh node stability, we computed for each node the registration error as the euclidean distance between nodes with the same indices from different analyses as well as the point-to-surface distance (distance from a point to the closest point on the mesh, that might lie inside a face) for every node. For visualisation, we show the mean point-to-point (resp point-to-surface) error map, averaged over the different individuals. This map was plotted over a template mesh, which was the population mean shape computed via Generalised Partial Procrustes Analysis (Dean, 2000).

Since the test/retest segmentations come from different images, we cannot use the previous metrics that depend on image coordinates. Therefore, we assessed the resulting 3D models only qualitatively.

3.3 Reproducibility of the parcellation method

The RV parcellation provided by our method is dependent on the RV segmentation, whose variability was assessed in the previous section. Therefore, even if the method is automatic and 100% reproducible under the same image and segmentation, we need to evaluate the robustness of the method to the segmentation variability that is present in a normal clinical setting.

We used the re-analysed dataset to test the reproducibility of the regional volumes and EF in the inter- and intra- observer tests. We report the mean and percent absolute difference in volumes and EF. For the data obtained in the test-retest setting, we report the regional volumes for both acquisitions, as well as the absolute and percent differences.

3.4 Validation of the parcellation method

To validate our method, given the lack of a clinical ground truth, we remodelled a template shape synthetically, both locally and globally. Since we imposed the remodelling, we know the specific areas as well as the exact amount of remodelling, computed as the global difference in volume between the template and the remodelled meshes.

For each RV segment (apical, inlet, outflow), we generate two local remodelling patterns: one elongating in the longitudinal direction, and the other in the circumferential. This remodelling is generated using the log-domain reconstruction method. This method needs as input the mesh topology, the rotation between faces R_{ij} and the in-triangle coordinates for each node a_{ti} . The topology and R_{ij} variables are the same as of the reference mesh. We define the equation governing the remodelled coordinates a_{ti} in terms of the in-triangle coordinates of the reference mesh a_{ti}^{ref} and the strain $\epsilon_4(\lambda)$, which will be defined in the upcoming paragraph

$$a_{ti} - a_{tj} = (Id + \epsilon_t(\lambda)) (a_{ti}^{ref} - a_{tj}^{ref}) \quad (28)$$

The strain ϵ_t is localised by imposing a decay on the desired strain magnitude: the strain at each triangle decays proportional to a Gaussian function of the distance from the centre of the triangle to the anatomical landmark defining the segment (apex, tricuspid, pulmonary valve). The strain matrix at each triangle are defined as follows:

$$\epsilon_t(\lambda) = \lambda(v_t \otimes v_t) \exp \frac{d_M(x)^2}{\omega^2} \quad (29)$$

Where v_t corresponds to either the longitudinal or circumferential direction (defined in section 2.2) at triangle t , λ is a parameter that controls the remodelling amount and is chosen to satisfy a certain increment in volume (from 1 to 5 ml) via the regula falsi method. The bandwidth ω is chosen to be 15mm. The valves' annuli are composed of fibrous tissue and do not show much

Table 1: Intra and inter-observer variability (in ml and percent) of the segmentations and node positions.

	Interobserver	Intraobserver
Volume difference	11.0ml (7%)	5.0ml (3.3%)
Dice coefficient	0.71	0.89
Mean node error	7.6mm \pm 2.3mm	6.2 \pm 1.5
Mean point-to-surface error	1.8mm \pm 1.0mm	1.3mm \pm .5mm

remodelling in most cases (though they can passively stretch in severe volume overload). Since this localised model is primarily aimed to assess short-term remodelling only, the strain is set at 0 in the triangles corresponding to a valve.

The global remodelling was generated by applying the linear transformation corresponding to a scaling range that increases from 0% to 10% the global volume.

We applied our parcellation method to the template mesh and the remodelled meshes. Afterwards, we compute the differences in regional volumes from the template, and assess our method’s accuracy. The global remodelling homogeneously affects all regions: the volume percentages of each region have to be preserved. The local remodelling only affects one region, and therefore only the deformed region must increase its volume.

4 Results

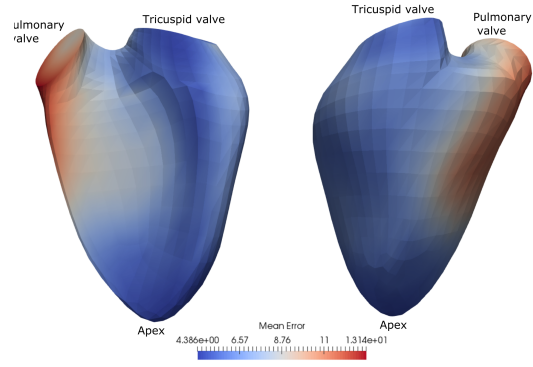
4.1 Regional and global volumes of our population

Table S1 shows the regional and global volumes, as well as the EF and the heart rate (HR) of all individuals composing our test populations. All generated 3D models and associated parcellations can be seen in Figure S1. There is high variability in both the global shape and the volumes, especially in the basal part of the inlet and outflow tract. Visually, the apical segment presents less variability, but the connecting region between the inlet and outflow presents more heterogeneity.

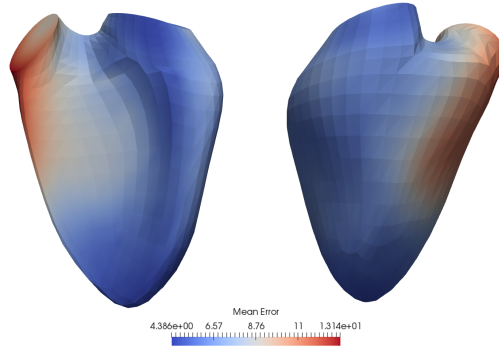
4.2 Reproducibility of the 3D models

Here we present the analysis of the inter- and intra-observer reproducibility of the ED shapes, as acquired from 3D echocardiography, as well as a qualitative discussion on the test/retest. Table 1 shows the mean error of the different metrics to assess shape differences: total volume difference, Dice coefficient and mean point-to-point and point-to-surface distances. As expected, interobserver reproducibility was lower than intraobserver. The total volume error was below 10% for both inter- and intra-observer, but the other metrics, that evaluated local differences, indicated lower stability. In particular, the interobserver Dice coefficient(0.71) was considerably lower than the intraobserver one (0.89).

Figure 4 shows the regional mean inter- and intra-observer point-to-point distance. We can see that the anterior insertion points, specially near the right ventricular outflow tract (RVOT), presents a higher level of instability with mean distances above 1cm. Instability is not only present in the anterior wall, but also affects the septum. Figure 5 shows the mean error using the point-to-surface distance instead of the point-to-point, thus assessing the stability of the contours independently of the node placement. The mean error is lower compared to the point-to-point case and contained to the outflow.

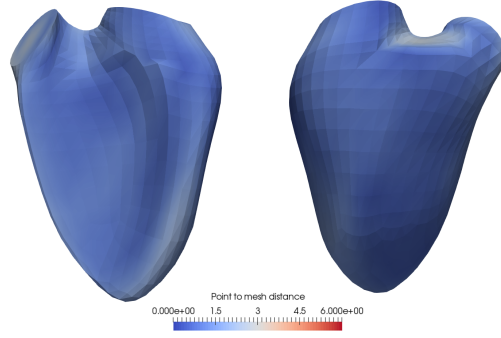


(a) Intraobserver reproducibility

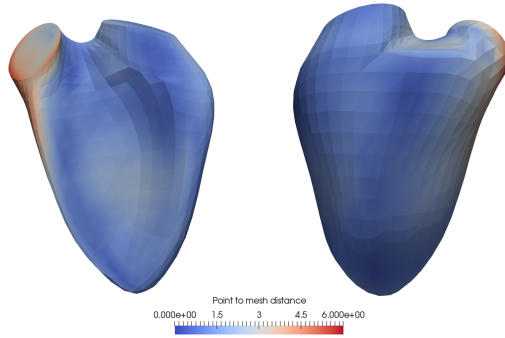


(b) Interobserver reproducibility

Figure 4: Mean point-to-point registration error for each node on the interobserver and intraobserver reproducibility test. We can see that the biggest errors are concentrated near the outflow tract, and in the anterior wall. The posterior wall and apical regions are more stable.



(a) Intraobserver reproducibility



(b) Interobserver reproducibility

Figure 5: Mean point-to-surface distance for each node on the interobserver and intraobserver reproducibility test. The errors are much lower than the point-to-point case, and concentrated in the boundaries, specially the outflow tract, and a fragment of the posterior wall near the apex that is usually cut in the images.

Table 2: Intra- and inter-observer variability of the segmental and total end-diastolic volumes and EF, expressed as the mean error and mean percent error (in parenthesis).

	Interobserver error	Intraobserver error	Mean value
RV EDV [ml]	4.98(3.34%)	10.96(7.01%)	144
Outflow ED V[ml]	3.43(10.00%)	9.03(22.19%)	36
Inlet EDV [ml]	3.27(04.08%)	09.26(12.21%)	68
Apical EDV [ml]	1.82(05.34%)	3.46(08.98%)	39
RV EF [%]	2.4 (4.9%)	5.2(10.1%)	50
Outflow EF	3.1 (7.9%)	10.6(23.2%)	42
Inlet EF	3.2 (6.9%)	5.1(10.6%)	50
Apical EF	5.2 (9.2%)	08.6(14.7%)	61

Table 3: Regional volumes resulting from two consecutive acquisitions of the same patient.

	Outflow (ml)	Inlet (ml)	Apex (ml)
Acquisition #1	20.81	50.82	18.64
Acquisition #2	22.45	47.51	20.0
Absolute error	1.64	3.25	1.40
Relative error	7.5%	6.8%	7.3%

Figure 6 shows the 3D models generated from the test/retest experiment and their parcellations. Differences in the parcellations will be described in next subsection. Both meshes have the same total volume, but differ in shape: acquisition #2 has a higher tricuspid valve and in acquisition #1 the pulmonary valve is further. Also, acquisition #1 presents a displaced anterior insertion "line". Acquisition #2 segmentation has a wider septum, that extends further in the anterior segment. Acquisition #2 has a more spherical apex and a flatter posterior wall.

4.3 Reproducibility of the parcellation method

In this section we report the stability of the measurements obtained with the proposed parcellation method. Reproducibility was estimated using the meshes obtained from the data used for the inter- and intra-observer reproducibility test. Table 2 shows the mean intra- and inter-observer errors and the mean value of the variables for the regional and global ED volumes and EF. We can observe large errors in the interobserver case ($>12\%$), but lower for the intraobserver case ($4 - 10\%$). The outlet segment had the biggest error for volume(10%), and regarding function, the apical EF has the biggest error.

We used the test/retest acquisition to verify whether the level of noise is higher in that situation. The two generated 3D models can be found in Figure 6, and we can see clear differences in shape. Table 3 shows the quantitative analysis of the regional volume differences. The errors found in the test/retest experiment corresponded to the ones observed in the intraobserver reproducibility test.

4.4 Validation of the parcellation method

We used the synthetic remodelling method to generate different types of localised and global remodelling in the longitudinal and circumferential directions. As template we used the mean

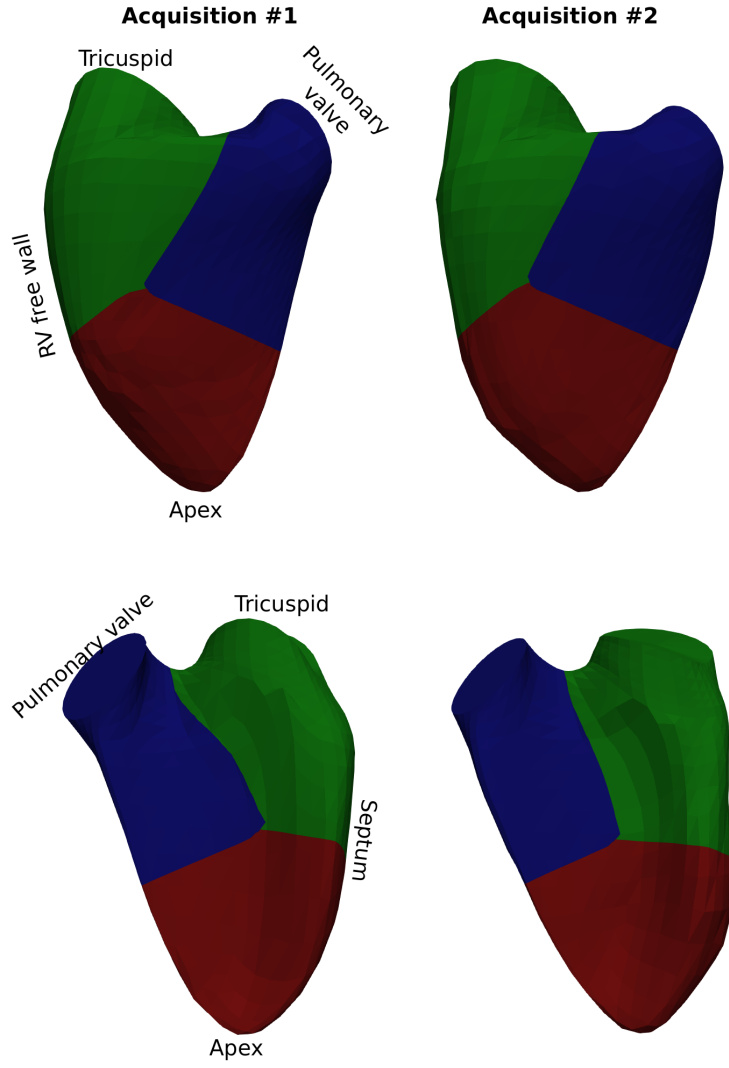


Figure 6: The two generated 3D models and their parcellations. Even if they have the same approximate size, they have significant differences especially in the anterior wall. These regional differences in the 3D models affects the parcellations: the biggest parcellation differences are in the center of the septum and free wall.

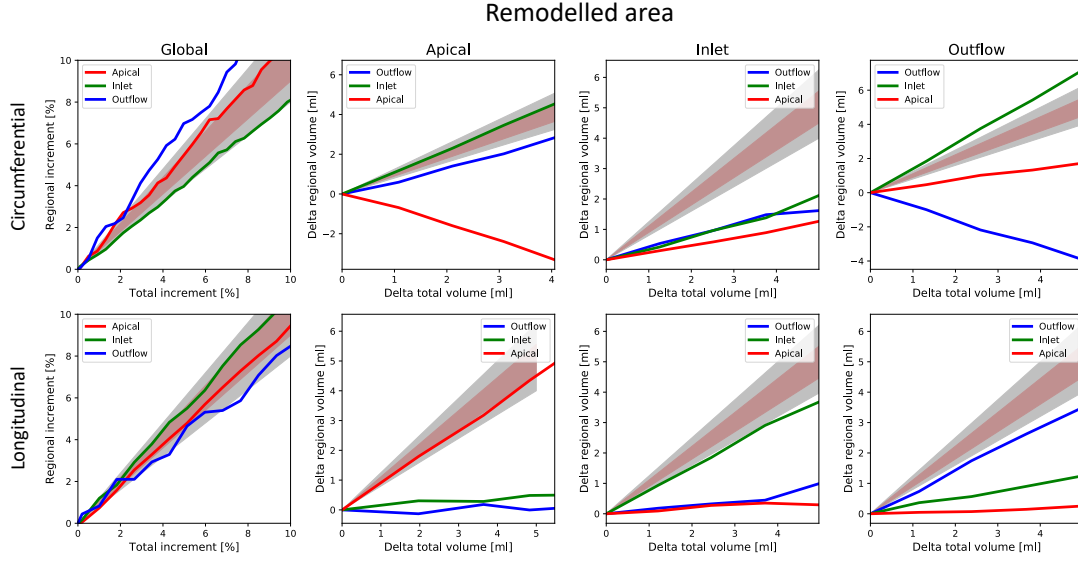


Figure 7: Regional volume differences between the synthetically remodelled meshes and the reference RV, for both regional and global. The regional remodelling consists of an increment of up to 5ml in a certain region only. We can see that the method is able to capture between 90% and 80% of the circumferential remodelling, but is not able to identify the procedence of longitudinal remodelling.

shape of our population, obtained using the Partial Generalised Procrustes Analysis. The local remodelling scaling parameters are set to obtain a total volume increase between 1 to 5ml, with increments of 1ml. All combinations of affected part (apical, inlet or outflow) and direction (longitudinal or circumferential) were tested, and resulting surfaces corresponding to 5ml are shown in Figure S3 of the supplementary material. For each combination of part and direction, 10 meshes were generated using the global remodelling method, its volume increase ranging from 0% to 10%. An example of the generated meshes using this method can be seen in Figure S2.

The first column of Figure ?? shows the regional dilatation (%) response to a global circumferential and longitudinal scaling. The expected output is that all regions increase their volume in the same proportion, which corresponds to the identity line. We can see that global remodelling distributes quite homogeneously for both longitudinal and circumferential remodelling (with a 90% accuracy), with circumferential scaling presenting a much lower noise than longitudinal scaling. Note that, by construction, the result of a pure scaling maintains exactly the volume proportions. Among the different regions, the outflow presents bigger variability. The other columns of Figure 7 show the changes of regional volumes after applying the local synthetic remodelling. The desired result is that all of the volume increment is located in the segment that suffers the remodelling (identity line), and the other segments do not change their volume. We see that circumferential remodelling is mostly associated to the correct segment (80 – 90%) in the apex and inlet, while the method is not suited to capture local longitudinal elongations.

5 Discussion

In this paper we proposed a mesh-independent method to volumetrically parcellate the RV in three clinically relevant regions: inlet, outlet and apex, with the aim to quantify inter- or intra-individual remodelling in regional morphology.

For validation, we additionally presented a method to synthetically remodel meshes in a localised and global manner, thus generating a synthetic dataset resembling closely monitoring clinical remodelling. From these, we found that the parcellation had a good sensitivity to circumferential or global remodelling, able to attribute it to the correct segment (80-90% of the volume was assigned to the correct segment). However, our method is less accurate when analysing local longitudinal localised remodelling. This is not a major problem given that in many clinical scenarios, regional volume and shape remodelling is often in the circumferential direction (D’Ascenzi et al., 2016).

We studied the variability of the semiautomatic RV segmentations. The interobserver reproducibility test of meshes resulting from the segmentation of 3D echocardiography, showed that, even if the mean volume difference was under 10%, the inter-observer Dice coefficient was very low (0.71). This implies that RV shapes segmented by different operators cannot be directly compared and pooled together in an analysis. On the other hand, the intraobserver reproducibility was much higher using the same image (Dice coefficient = 0.89). A test/retest experiment presented significant visual differences. Moreover, the point-to-point (6.2mm) error was much higher than the point-to-surface (1.3mm): the interior nodes of the mesh do not correspond to any anatomical landmark but are equally distributed, thus their correct position does not depend only on the correct segmentation of the RV contour in their position, but on the whole segmentation.

This RV variability influences the resulting parcellation, since it is derived from the generated 3D model. Therefore, interobserver reproducibility of the regional volumes and EF also present a high error ($>10\%$). On the other hand, the intraobserver reproducibility presented less error: in volumes only the outflow had a variability $\geq 10\%$, while inlet and apex were below (4% and 5%) respectively. The outflow is complicated to segment given the images there often have lower quality. A qualitative analysis of the partitions showed big differences in the middle of the RV since this is the furthest from all landmarks and the method has no information to make the exact parcellation. The inclusion of anatomical landmarks in that area could improve the reproducibility of the method. Regarding the EF, the most unstable was the apical part. This is likely caused by the presence of trabeculations introducing variability in the segmentation as well as the nearfield effect playing a role there and making the full visualisation of the apex challenging.

6 Conclusion

We proposed a geometry processing method to parcellate the RV in 3 regions: inlet, outlet and apical, for analysing regional morphology of the RV without depending on point-to-point correspondence of image-based segmented meshes. This parcellation also allowed to assess function via regional EF. We analysed the reproducibility of the regional measurements, and found it below 8% in both apex and inlet segments for the intraobserver, but above 12% in the interobserver case and outflow. Given that most of the instability comes from segmentation errors in the outflow portion, the addition of extra landmarks (like for example in the middle of the septum) would allow to improve reproducibility. We also proposed and used a novel method to generate localised remodelling patterns. We used it to generate synthetic remodelling surfaces to validate our parcellation method and showed that it captures global scaling of the ventricles as well as

localised remodelling in the circumferential directions, but has difficulties in local longitudinal elongations.

Acknowledgements

This study was partially supported by the Spanish Ministry of Economy and Competitiveness (Maria de Maeztu Units of Excellence Programme - MDM-2015-0502), the European Union under the Horizon 2020 Programme for Research, Innovation (grant agreement No. 642676 CardioFunXion).

References

- Karima Addetia, Francesco Maffessanti, Megan Yamat, Lynn Weinert, Akhil Narang, Benjamin H. Freed, Victor Mor-Avi, and Roberto M. Lang. Three-dimensional echocardiography-based analysis of right ventricular shape in pulmonary arterial hypertension. *European Heart Journal – Cardiovascular Imaging*, 17(5):564–575, 5 2016. ISSN 2047-2404. doi: 10.1093/ehjci/jev171. URL <https://academic.oup.com/ehjcardimaging/article-lookup/doi/10.1093/ehjci/jev171>.
- Karima Addetia, Francesco Maffessanti, Denisa Muraru, Amita Singh, Elena Surkova, Victor Mor-Avi, Luigi P. Badano, and Roberto M. Lang. Morphologic Analysis of the Normal Right Ventricle Using Three-Dimensional Echocardiography-Derived Curvature Indices. *Journal of the American Society of Echocardiography*, 31(5):614–623, 5 2018. ISSN 08947317. doi: 10.1016/j.echo.2017.12.009. URL <https://linkinghub.elsevier.com/retrieve/pii/S0894731717308830>.
- T Arts, F W Prinzen, L H E H Snoeckx, J M Rijcken, and R S Reneman. Adaption of cardiac structure by mechanical feedback in the environment of the cell: A model study. *Biophysical Journal*, 66(4):953–961, 1994. ISSN 00063495. doi: 10.1016/S0006-3495(94)80876-8. URL [http://dx.doi.org/10.1016/S0006-3495\(94\)80876-8](http://dx.doi.org/10.1016/S0006-3495(94)80876-8).
- G. Auzias, J. Lefevre, A. Le Troter, C. Fischer, M. Perrot, J. Regis, and O. Coulon. Model-driven harmonic parameterization of the cortical surface: HIP-HOP. *IEEE Transactions on Medical Imaging*, 2013. ISSN 02780062. doi: 10.1109/TMI.2013.2241651.
- A Baltaeva, M Marcinak, B Bijmens, J Moggridge, F He, T Antonios, G MacGregor, and G Sutherland. Regional left ventricular deformation and geometry analysis provides insights in myocardial remodelling in mild to moderate hypertension. *European Journal of Echocardiography*, 10 2007. ISSN 15252167. doi: 10.1016/j.euje.2007.08.004. URL <https://academic.oup.com/ehjcardimaging/article-lookup/doi/10.1016/j.euje.2007.08.004>.
- Oualid M. Benkarim, Gemma Piella, Nadine Hahner, Elisenda Eixarch, Miguel Angel González Ballester, and Gerard Sanroma. Patch spaces and fusion strategies in patch-based label fusion. *Computerized Medical Imaging and Graphics*, 2019. ISSN 18790771. doi: 10.1016/j.compmedimag.2018.11.004.
- Manuel D. Cerqueira, Neil J. Weissman, Vasken Dilsizian, Alice K. Jacobs, Sanjiv Kaul, Warren K. Laskey, Dudley J. Pennell, John A. Rumberger, Thomas J. Ryan, and Mario S. Verani. Standardized myocardial segmentation and nomenclature for tomographic imaging of the heart. *Journal of Cardiovascular Magnetic Resonance*, 2002. ISSN 10976647. doi: 10.1081/JCMR-120003946.

- Maja Cikes, George R. Sutherland, Lisa J. Anderson, and Bart H. Bijmens. The role of echocardiographic deformation imaging in hypertrophic myopathies. *Nature Reviews Cardiology*, 7(7):384–396, 2010. ISSN 17595002. doi: 10.1038/nrcardio.2010.56.
- Robert Cimrman, Vladimír Lukeš, and Eduard Rohan. Multiscale finite element calculations in Python using SfePy. *Advances in Computational Mathematics*, 45(4):1897–1921, 8 2019. ISSN 1019-7168. doi: 10.1007/s10444-019-09666-0. URL <http://link.springer.com/10.1007/s10444-019-09666-0>.
- Flavio D’Ascenzi, Antonio Pelliccia, Domenico Corrado, Matteo Cameli, Valeria Curci, Federico Alvinio, Benedetta Maria Natali, Marta Focardi, Marco Bonifazi, and Sergio Mondillo. Right ventricular remodelling induced by exercise training in competitive athletes. *European Heart Journal – Cardiovascular Imaging*, 17(3):301–307, 3 2016. ISSN 2047-2404. doi: 10.1093/ehjci/jev155. URL <https://academic.oup.com/ehjcardimaging/article-lookup/doi/10.1093/ehjci/jev155>.
- David Dean. Statistical Shape Analysis. *Journal of Human Evolution*, 38(3):455–457, 3 2000. ISSN 00472484. doi: 10.1006/jhev.1999.0391. URL <https://linkinghub.elsevier.com/retrieve/pii/S0047248499903913>.
- J. E. Dennis, Jr. and Jorge J. Moré. Quasi-Newton Methods, Motivation and Theory. *SIAM Review*, 19(1):46–89, 1 1977. ISSN 0036-1445. doi: 10.1137/1019005. URL <http://epubs.siam.org/doi/10.1137/1019005>.
- Ruben Doste, David Soto-Iglesias, Gabriel Bernardino, Alejandro Alcaine, Rafael Sebastian, Sophie Giffard-Roisin, Maxime Sermesant, Antonio Berruezo, Damian Sanchez-Quintana, and Oscar Camara. A rule-based method to model myocardial fiber orientation in cardiac biventricular geometries with outflow tracts. *International Journal for Numerical Methods in Biomedical Engineering*, 35(4):e3185, 4 2019. ISSN 2040-7939. doi: 10.1002/cnm.3185. URL <https://onlinelibrary.wiley.com/doi/abs/10.1002/cnm.3185>.
- Yabo Fu, Yang Lei, Tonghe Wang, Walter J. Curran, Tian Liu, and Xiaofeng Yang. Deep Learning in Medical Image Registration: A Review. 12 2019. URL <http://arxiv.org/abs/1912.12318>.
- Guillermo Gallego and Anthony Yezzi. A Compact Formula for the Derivative of a 3-D Rotation in Exponential Coordinates. *Journal of Mathematical Imaging and Vision*, 51(3):378–384, 3 2015. ISSN 0924-9907. doi: 10.1007/s10851-014-0528-x. URL <http://link.springer.com/10.1007/s10851-014-0528-x>.
- W. Grossman, D. Jones, and L. P. McLaurin. Wall stress and patterns of hypertrophy in the human left ventricle. *Journal of Clinical Investigation*, 56(1):56–64, 7 1975. ISSN 0021-9738. doi: 10.1172/JCI108079. URL <http://www.jci.org/articles/view/108079>.
- David Xianfeng Gu, Feng Luo, and Shing-Tung Yau. Fundamentals of Computational Conformal Geometry. *Mathematics in Computer Science*, 4(4):389–429, 12 2010. ISSN 1661-8270. doi: 10.1007/s11786-011-0065-6. URL <http://link.springer.com/10.1007/s11786-011-0065-6>.
- Francois Haddad, Ramona Doyle, Daniel J. Murphy, and Sharon A. Hunt. Right Ventricular Function in Cardiovascular Disease, Part II. *Circulation*, 117(13):1717–1731, 4 2008a. ISSN 0009-7322. doi: 10.1161/CIRCULATIONAHA.107.653584. URL <https://www.ahajournals.org/doi/10.1161/CIRCULATIONAHA.107.653584>.

- Francois Haddad, Sharon A. Hunt, David N. Rosenthal, and Daniel J. Murphy. Right Ventricular Function in Cardiovascular Disease, Part I. *Circulation*, 117(11):1436–1448, 3 2008b. ISSN 0009-7322. doi: 10.1161/CIRCULATIONAHA.107.653576. URL <https://www.ahajournals.org/doi/10.1161/CIRCULATIONAHA.107.653576>.
- A Hamdy. Use of strain and tissue velocity imaging for early detection of regional myocardial dysfunction in patients with beta thalassemia. *European Journal of Echocardiography*, 8(2): 102–109, 3 2007. ISSN 15252167. doi: 10.1016/j.euje.2006.02.004. URL <https://academic.oup.com/ehjcmaging/article-lookup/doi/10.1016/j.euje.2006.02.004>.
- Monica K. Hurdal and Ken Stephenson. Discrete conformal methods for cortical brain flattening. *NeuroImage*, 45(1):S86–S98, 3 2009. ISSN 10538119. doi: 10.1016/j.neuroimage.2008.10.045. URL <https://linkinghub.elsevier.com/retrieve/pii/S1053811908011701>.
- S. Joshi, Brad Davis, Matthieu Jomier, and Guido Gerig. Unbiased diffeomorphic atlas construction for computational anatomy. *NeuroImage*, 23(SUPPL. 1), 2004. ISSN 10538119. doi: 10.1016/j.neuroimage.2004.07.068.
- B Lévy. Constrained Texture Mapping for Polygonal Meshes. *Proceedings of the 28th annual conference on Computer graphics and interactive techniques*, (August):12–17, 2001. ISSN 158113374X. doi: 10.1145/383259.383308. URL <http://dl.acm.org/citation.cfm?id=383308>.
- Pamela Mocerì, Nicolas Duchateau, Delphine Baudouy, Elie-Dan Schouver, Sylvie Leroy, Fabien Squara, Emile Ferrari, and Maxime Sermesant. Three-dimensional right-ventricular regional deformation and survival in pulmonary hypertension. *European Heart Journal - Cardiovascular Imaging*, 19(4):450–458, 4 2018. ISSN 2047-2404. doi: 10.1093/ehjci/jex163. URL <https://academic.oup.com/ehjcmaging/article/19/4/450/3868545>.
- Denisa Muraru, Veronica Spadotto, Antonella Cecchetto, Gabriella Romeo, Patrizia Aruta, Davide Ermacora, Csaba Jenei, Umberto Cucchini, Sabino Iliceto, and Luigi P. Badano. New speckle-tracking algorithm for right ventricular volume analysis from three-dimensional echocardiographic data sets: validation with cardiac magnetic resonance and comparison with the previous analysis tool. *European heart journal cardiovascular Imaging*, 2016. ISSN 20472412. doi: 10.1093/ehjci/jev309.
- Petra S. Niemann, Luiz Pinho, Thomas Balbach, Christian Galuschky, Michael Blankenhagen, Michael Silberbach, Craig Broberg, Michael Jerosch-Herold, and David J. Sahn. Anatomically Oriented Right Ventricular Volume Measurements With Dynamic Three-Dimensional Echocardiography Validated by 3-Tesla Magnetic Resonance Imaging. *Journal of the American College of Cardiology*, 50(17):1668–1676, 10 2007. ISSN 07351097. doi: 10.1016/j.jacc.2007.07.031. URL <https://linkinghub.elsevier.com/retrieve/pii/S073510970702462X>.
- Jorge Nocedal. Updating Quasi-Newton Matrices with Limited Storage. *Mathematics of Computation*, 35(151):773, 7 1980. ISSN 00255718. doi: 10.2307/2006193. URL <https://www.jstor.org/stable/2006193?origin=crossref>.
- Marta Nuñez-Garcia, Gabriel Bernardino, Ruben Doste, Jichao Zhao, Oscar Camara, and Constantine Butakoff. Standard Quasi-Conformal Flattening of the Right and Left Atria. In *Lecture Notes in Computer Science (including subseries Lecture Notes in Artificial Intelligence and Lecture Notes in Bioinformatics)*, pages 85–93. 2019. ISBN 9783030219482. doi: 10.1007/978-3-030-21949-9_{_}10. URL http://link.springer.com/10.1007/978-3-030-21949-9_10.

- Iacopo Olivotto, Franco Cecchi, Corrado Poggesi, and Magdi H. Yacoub. Patterns of Disease Progression in Hypertrophic Cardiomyopathy. *Circulation: Heart Failure*, 5(4):535–546, 7 2012. ISSN 1941-3289. doi: 10.1161/CIRCHEARTFAILURE.112.967026. URL <https://www.ahajournals.org/doi/10.1161/CIRCHEARTFAILURE.112.967026>.
- Lionel H. Opie, Patrick J. Commerford, Bernard J. Gersh, and Marc A. Pfeffer. Controversies in ventricular remodelling. *The Lancet*, 367(9507):356–367, 1 2006. ISSN 01406736. doi: 10.1016/S0140-6736(06)68074-4. URL <https://linkinghub.elsevier.com/retrieve/pii/S0140673606680744>.
- Bruno Paun, Bart Bijmens, Tinen Iles, Paul A. Iaizzo, and Constantine Butakoff. Patient independent representation of the detailed cardiac ventricular anatomy. *Medical Image Analysis*, 2017. ISSN 13618423. doi: 10.1016/j.media.2016.07.006.
- Ulrich Pinkall and Konrad Polthier. Computing Discrete Minimal Surfaces and Their Conjugates. *Experimental Mathematics*, 2(1):15–36, 1 1993. ISSN 1058-6458. doi: 10.1080/10586458.1993.10504266. URL <http://www.tandfonline.com/doi/abs/10.1080/10586458.1993.10504266>.
- Hang Si. TetGen, a Delaunay-Based Quality Tetrahedral Mesh Generator. *ACM Transactions on Mathematical Software*, 41(2):1–36, 2 2015. ISSN 00983500. doi: 10.1145/2629697. URL <http://dl.acm.org/citation.cfm?doid=2732672.2629697>.
- Olga Sorkine and Marc Alexa. As-Rigid-As-Possible Surface Modeling. *Proceedings of the fifth Eurographics symposium on Geometry processing*, 2007. ISSN 10009000. doi: 10.1007/s11390-011-1154-3.
- Vitaly Surazhsky, Tatiana Surazhsky, Danil Kirsanov, Steven J. Gortler, and Hugues Hoppe. Fast exact and approximate geodesics on meshes. In *ACM SIGGRAPH 2005 Papers on - SIGGRAPH '05*, page 553, New York, New York, USA, 2005. ACM Press. doi: 10.1145/1186822.1073228. URL <http://portal.acm.org/citation.cfm?doid=1186822.1073228>.
- Sergio Vera, Miguel A. González Ballester, and Debora Gil. Anatomical parameterization for volumetric meshing of the liver. In Ziv R. Yaniv and David R. Holmes, editors, *Medical Imaging 2014: Image-Guided Procedures, Robotic Interventions, and Modeling*, page 903605, 3 2014. ISBN 9780819498298. doi: 10.1117/12.2043572. URL <http://proceedings.spiedigitallibrary.org/proceeding.aspx?doi=10.1117/12.2043572>.
- Y Wang, B Liu, and Y Tong. Linear Surface Reconstruction from Discrete Fundamental Forms on Triangle Meshes. 0(0):1–10, 2012. URL <https://www.cse.msu.edu/~ytong/DiscreteFundamentalForms.pdf>.
- Xingyu Zhang, Pau Medrano-Gracia, Bharath Ambale-Venkatesh, David A. Bluemke, Brett R. Cowan, J. Paul Finn, Alan H. Kadish, Daniel C. Lee, Joao A. C. Lima, Alistair A. Young, and Avan Suinesiaputra. Orthogonal decomposition of left ventricular remodeling in myocardial infarction. *GigaScience*, 6(3), 3 2017. ISSN 2047-217X. doi: 10.1093/gigascience/gix005. URL <https://academic.oup.com/gigascience/article/doi/10.1093/gigascience/gix005/2968356>.

A Individual results

In this section we provide the individualised results of the parcellation for the 10 participants of the study. Table S1 shows the regional and global volume and ejection fraction of each subject. Figure shows the parcellation derived from all subjects.

Table S1: Global and regional RV volumes and ejection fraction of the full population.

	Outflow	EDV [ml		RV	Outflow	EF [%]		RV	HR [bpm]
		Inlet	Apex]			Inlet	Apex		
#1	36.1	95.6	34.3	165.9	47.3	52.3	66.1	54.0	53
#2	38.8	62.2	30.4	131.4	41.6	53.6	63.9	52.4	45
#3	32.0	80.4	30.6	142.9	35.5	41.2	57.7	43.4	58
#4	37.5	88.3	39.0	164.8	49.1	57.4	64.3	57.1	48
#5	44.7	84.1	38.2	167.0	47.7	52.4	70.5	55.3	56
#6	28.9	65.0	32.5	126.4	42.4	47.7	38.7	44.2	68
#7	25.9	78.3	29.9	134.1	34.2	47.2	58.2	47.1	50
#8	39.4	80.0	41.5	160.8	28.1	36.9	55.0	39.4	45
#9	31.1	77.9	28.1	137.0	45.7	51.2	59.1	51.6	63
#10	34.4	81.0	40.9	156.3	46.5	47.7	72.2	53.9	65

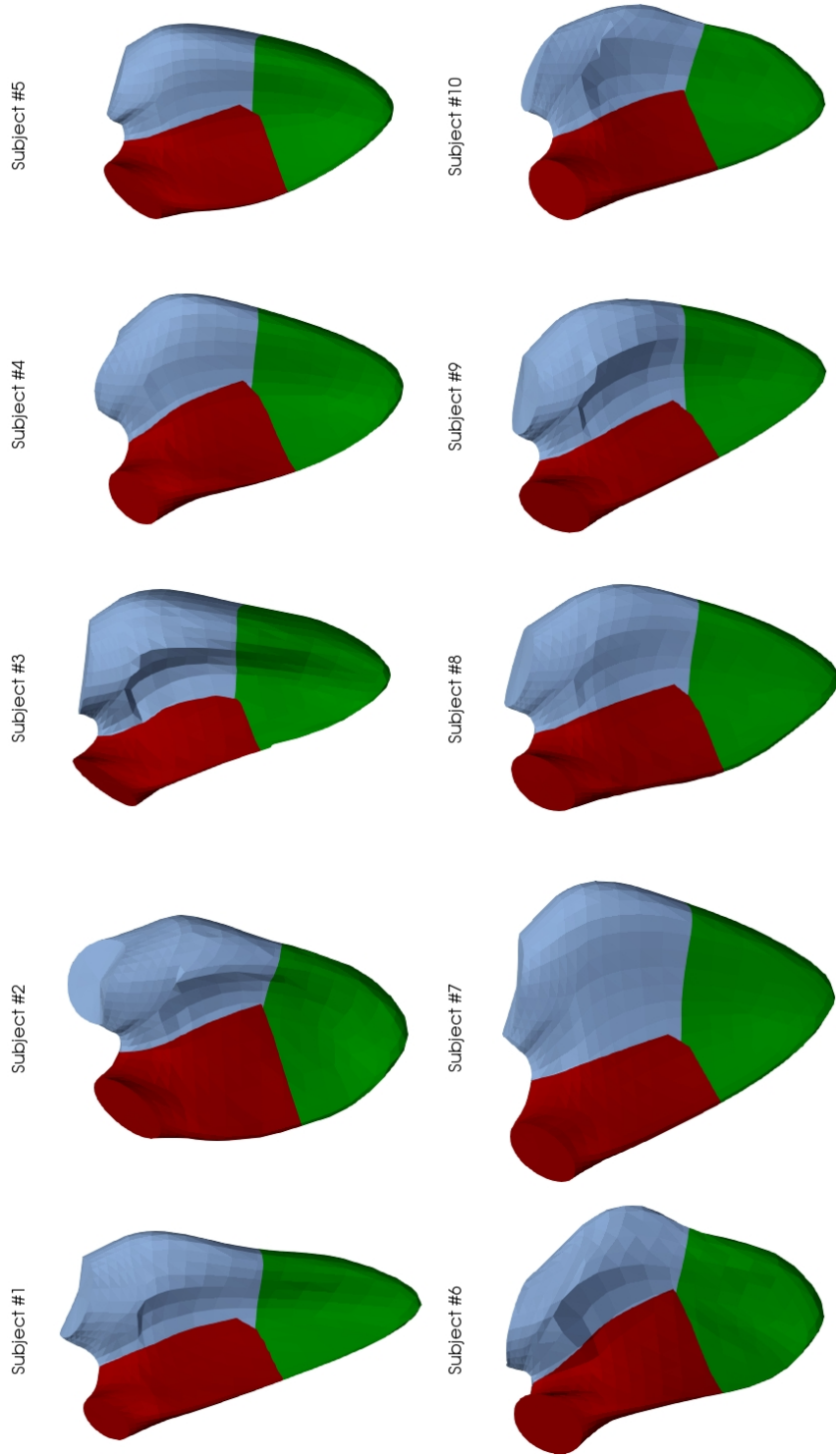


Figure S1: Parcellation and 3D models of all individuals of the population in apical (red), outflow (blue) and inlet (green). We can observe that there is a big variability in size and shape of the RV, which is reflected in the parcellation differences.

B Synthetically generated meshes

In this section, we show the synthetically generated meshes that are used for validating the parcellation method. Figure S2 shows the globally remodelled meshes, corresponding to a 10% volume increase in the circumferential and longitudinal direction, computed using the linear method described in Section 2.4.4 of the main text. Figure S3 shows the meshes obtained using the reconstruction method of Section 2.4.3, and correspond to 5ml increase of a single region (apical/inlet/outflow) in the longitudinal or circumferential directions.

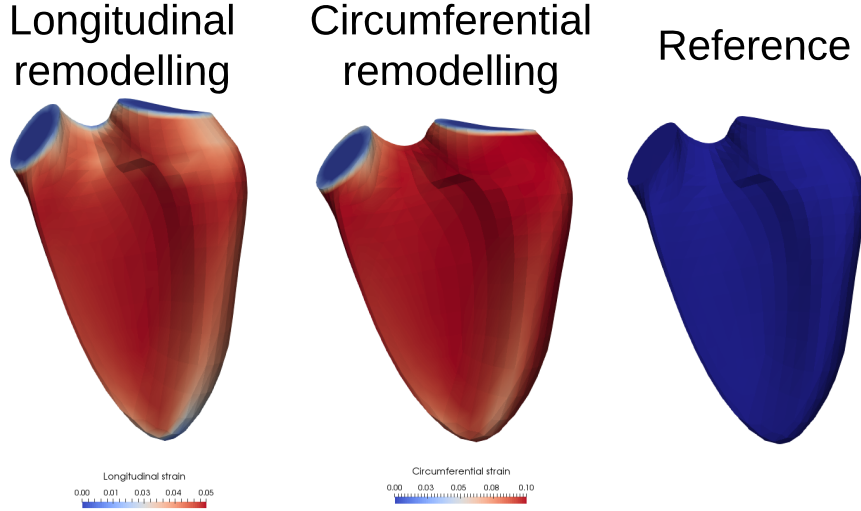


Figure S2: Generated RV meshes for the global synthetic remodelling, corresponding to a 10% dilation in both the longitudinal and circumferential. The colour map shows the strain of the deformation from the reference mesh.

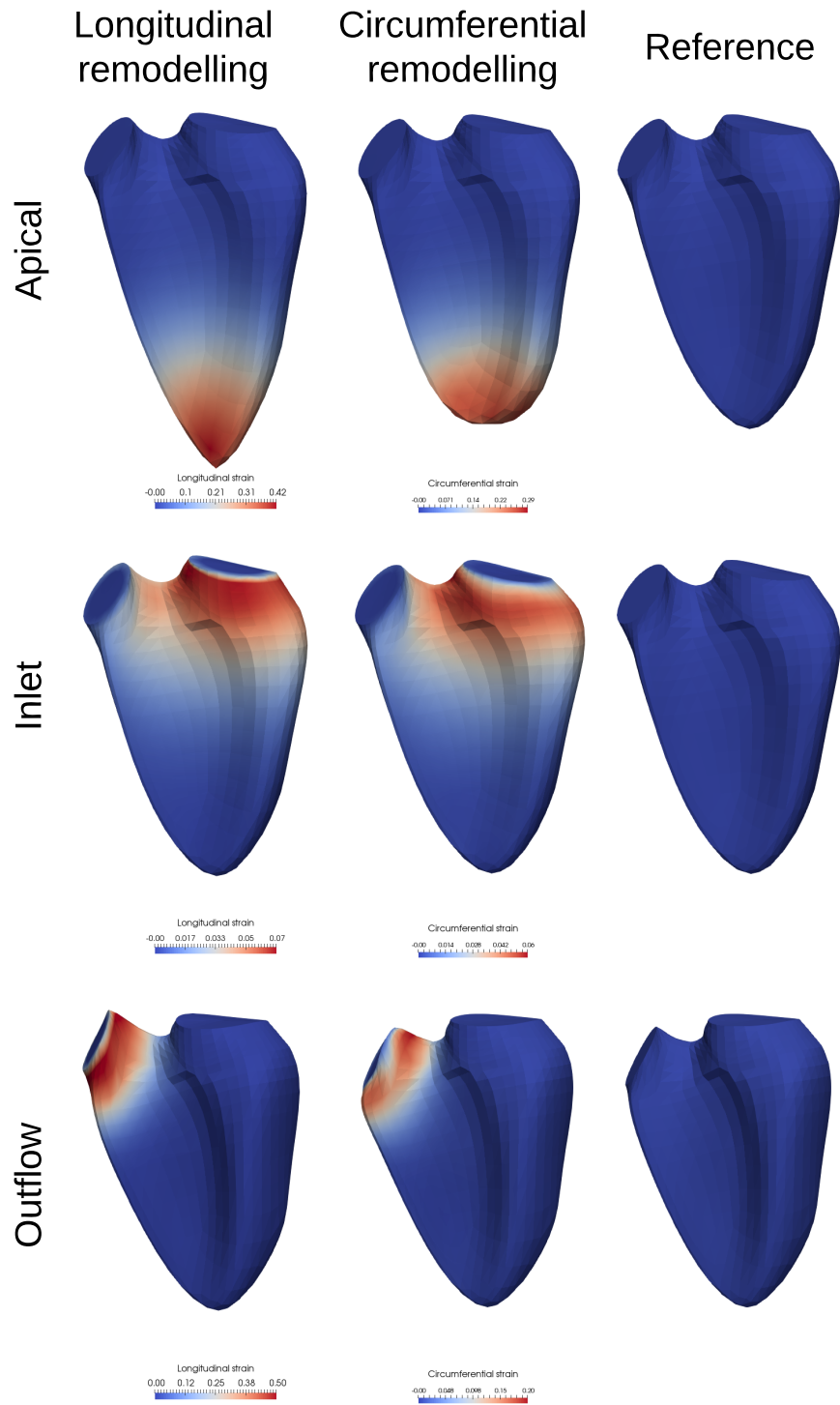


Figure S3: Generated meshes with the local synthetic remodelling method. The colour map shows the longitudinal / circumferential strain with respect to the reference, which is showed in the right column.